

Unsupervised Visual Chain-of-Thought Reasoning via Preference Optimization

Kesen Zhao¹ Beier Zhu^{1*} Qianru Sun² Hanwang Zhang¹

¹Nanyang Technological University, ²Singapore Management University
kesen002@e.ntu.edu.sg, qianrusun@smu.edu.sg
{beier.zhu, hanwangzhang}@ntu.edu.sg

Abstract

Chain-of-thought (CoT) reasoning greatly improves the interpretability and problem-solving abilities of multimodal large language models (MLLMs). However, existing approaches are focused on text CoT, limiting their ability to leverage visual cues. Visual CoT remains underexplored, and the only work [28] is based on supervised fine-tuning (SFT) that relies on extensive labeled bounding-box data and is hard to generalize to unseen cases. In this paper, we introduce Unsupervised Visual CoT (UV-CoT), a novel framework for image-level CoT reasoning via preference optimization. UV-CoT performs preference comparisons between model-generated bounding boxes (one is preferred and the other is dis-preferred), eliminating the need for bounding-box annotations. We get such preference data by introducing an automatic data generation pipeline. Given an image, our target MLLM (e.g., LLaVA-1.5-7B) generates seed bounding boxes using a template prompt and then answers the question using each bounded region as input. An evaluator MLLM (e.g., OmniLLM-12B) ranks the responses, and these rankings serve as supervision to train the target MLLM with UV-CoT by minimizing negative log-likelihood losses. By emulating human perception—identifying key regions and reasoning based on them—UV-CoT can improve visual comprehension, particularly in spatial reasoning tasks where textual descriptions alone fall short. Our experiments on six datasets demonstrate the superiority of UV-CoT, compared to the state-of-the-art textual and visual CoT methods. Our zero-shot testing on four unseen datasets shows the strong generalization of UV-CoT. The code is available in https://kesenzhao.github.io/my_project/projects/UV-CoT.html.

1. Introduction

With the recent advancements in multimodal large language models (MLLMs) [3, 17, 18, 39], many efforts have been made to incorporate text CoT reasoning [8, 13, 34, 42] to handle complex vision-language tasks [36, 37, 43]. However, the visual understanding ability of MLLM is limited by fixed-granularity image processing, i.e., the MLLM can’t dynamically adjust focus across different spatial regions of the input image, even when guided by text CoT prompts [9]. This underscores the critical need to explicitly integrate visual cues into the CoT process.

A very recent work called Visual-CoT [28] has made an initial attempt towards this goal. The model is trained using supervised fine-tuning (SFT) with human-labeled bounding boxes that indicate the key image regions relevant to the question. Following this, it performs its multimodal CoT approach with human-annotated reasoning steps by associating textual inputs with the detected regions. An overview of Visual CoT is presented in Fig. 1. However, it has two key drawbacks: (1) it relies on large-scale, high-quality labeled data, making it costly and hard to scale; and (2) SFT learns only from positive examples (i.e., the labeled training data), limiting its ability to generalize to unseen or ambiguous scenarios where intermediate reasoning or dynamic interpretation is needed.

To address these issues, we introduce an Unsupervised approach to Visual CoT dubbed as UV-CoT. It has two key parts: data collection and model training. The data collection does not need human annotation, as it leverages the data generation and evaluation capabilities of pre-trained MLLMs. The model training is inspired by the idea of direct preference optimization (DPO). It is implemented with an adapted version of DPO to address specific limitations in capturing the degree of preference and fine-grained region-based reasoning when conducting visual CoT on MLLMs.

Our method UV-CoT, as shown in Fig. 1, differs from Visual CoT [28] by adopting an unsupervised approach with contrastive preference data. We design an automatic two-step pipeline to generate this data: 1) Region Generation: Given an image, the target model generates multi-

*Corresponding author

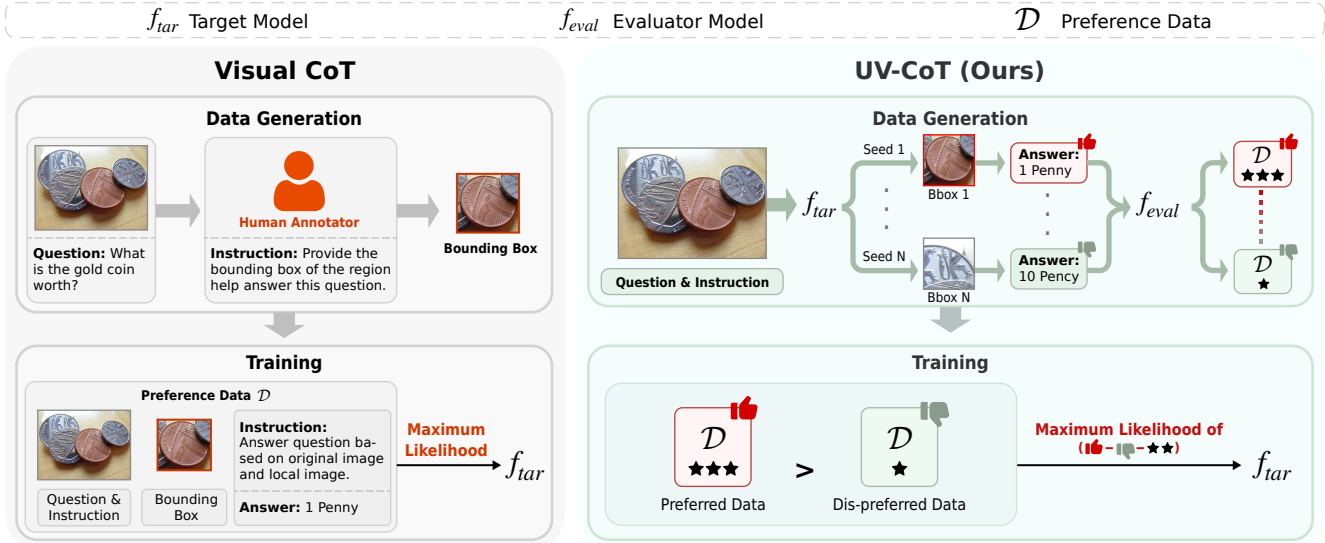


Figure 1. Comparison of Visual CoT [28] and our UV-CoT. **Left:** Visual CoT relies on human-annotated bounding boxes to identify key regions. The model is trained via supervised fine-tuning to maximize the likelihood of the labeled data. **Right:** UV-CoT eliminates the need for human annotation. Given an image, the target model generates seed bounding boxes and answers questions based on these regions, respectively. An evaluator MLLM then scores the responses as a proxy for assessing region quality. Lastly, the target model is optimized via preference optimization by maximizing the likelihood of preferred regions over dispreferred ones.

ple seed bounding boxes using a template prompt. It then answers the question by processing each bounded region together with the question as input. 2) Quality Assessment: An evaluator MLLM scores the responses, using these scores as proxies to measure the quality of the regions. Unlike traditional DPO, we propose Score-DPO (sDPO), which not only ranks preference data (i.e., preferred and dis-preferred responses shown in Fig. 1) but also assigns preference scores. This scoring enables more precise optimization based on score differences. During UV-CoT training, the rankings of the preference data act as supervision by minimizing negative log-likelihood loss, while the scores define the decision margin. By mimicking human perception—first identifying key regions, then reasoning over them—UV-CoT significantly improves visual comprehension, especially in spatial reasoning tasks where text-based methods fall short. By leveraging unsupervised data in a contrastive way, UV-CoT also shows strong generalization ability when tested on unseen datasets. We will show the evidence in the experimental sections.

Our contributions in this paper thus include: 1) an automatic pipeline for generating high-quality preference data, enabling robust and scalable preference learning of UV-CoT; 2) an improved version of DPO in UV-CoT by integrating the degree of preference for visual regions, allowing the model to distinguish key regions more precisely and improve its reasoning ability; and 3) extensive experiments on multiple challenging datasets, demonstrating state-of-the-art performance of UV-CoT on four benchmarks and

strong generalization to four unseen test datasets.

2. Related Works

Chain-of-Thought in LLMs and MLLMs. LLMs [3, 19, 32] show strong inferential abilities, with CoT [7, 34] improving their performance by guiding models through intermediate reasoning steps. Both manually designed [34] and self-generated [13, 42] reasoning approaches have proven effective in improving LLM performance. In contrast, MLLMs struggle with reasoning due to differences in processing textual and visual data. Multimodal CoT methods [36, 37, 43] attempt to address this by transforming multimodal inputs into a unified textual format, enabling LLMs to perform CoT at the text level. However, this transformation introduces significant information loss and prevents the models from capturing key visual details [43]. For example, LLaVA-CoT [36] leverages GPT-4o to summarize questions and image captions but suffers from weak optical character recognition and sometimes hallucinations.

A very recent work, Visual CoT [28], improves the MLLM reasoning by introducing CoT methods at the image level. This approach involves scanning the entire image, identifying key references, and then focusing the model on specific regions for reasoning. Despite its improvements, Visual CoT is heavily based on costly human-annotated data. In contrast, our UV-CoT framework utilizes unsupervised preference optimization with auto-generated preference data, eliminating the need for manual annotations.

Preference Learning in LLMs and MLLMs. RLHF [31]

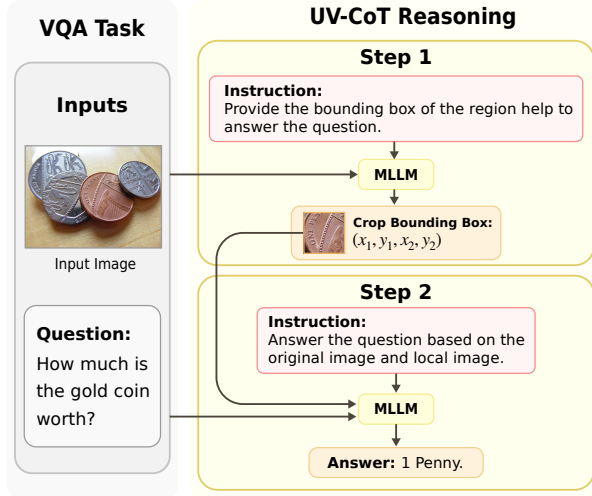


Figure 2. Illustration of UV-CoT reasoning.

aligns LLMs with human preferences by training a reward model via contrastive response evaluations [45]. To reduce reliance on human annotations, RLAIIF [15] leverages pre-trained LLMs for preference label generation. However, RL-based fine-tuning faces stability and efficiency challenges. Direct Preference Optimization (DPO) [26] addresses this by directly linking reward functions to optimal policies, eliminating reward model fine-tuning. Further improvements include IPO [2], which mitigates overfitting with a bounded preference function, and KTO [6], which removes the need for paired preference data, relying instead on single examples labeled as either “good” or “bad”.

These preference learning techniques are applied to MLLMs, with RLHF-V and RLAIIF-V [40, 41] refining behavior alignments using human and LLM-generated labels. To mitigate reward hacking, Sun et al. [30] enhance reward models with additional factual details, such as image captions and verified choices, further improving the performance of MLLM. Some works have attempted to apply DPO in the CoT process [14, 24]. However, these methods are designed for only text-level CoT and do not effectively handle visual features or cues. In contrast, in this paper, we propose UV-CoT, a specialized framework for image-level CoT reasoning inspired by the idea of DPO. Unlike traditional DPO, UV-CoT not only ranks preference data (i.e., preferred and dis-preferred data) but also assigns preference scores. This scoring enables more precise optimization of the MLLMs based on score differences.

3. Method

Fig. 1 illustrates the pipeline of UV-CoT reasoning. Given the original image and the question, we append a CoT prompt to guide the target MLLM in identifying the most informative image region and specifying its location via

Algorithm 1 Preference data generation for a query x

- 1: **Input:** Target model f_{tar} , evaluator f_{eval} , an image-question query x , number of seeds n , and number of preference pairs k .
 - 2: **Output:** Preference data \mathcal{D}
 - 3: Initialize $y_0 = x$
 - 4: **for** $t = 1$ to T **do**
 - 5: $\{y_t^i\}_{i=1}^n \leftarrow \text{Generate}(f_{\text{tar}}, y_{0:t-1}, n)$
 - 6: $\{s_t^i\}_{i=1}^n \leftarrow \text{Evaluate}(f_{\text{eval}}, y_{0:t-1}, \{y_t^i\}_{i=1}^n)$
 - 7: $\mathcal{D}_t \leftarrow \text{ConstructPairs}(y_{0:t-1}, \{y_t^i\}_{i=1}^n, \{s_t^i\}_{i=1}^n, k)$
 - 8: $y_t \leftarrow \text{Select}(y_{0:t-1}, \{y_t^i\}_{i=1}^n, \{s_t^i\}_{i=1}^n)$
 - 9: **end for**
 - 10: **return** $\mathcal{D} = \{\mathcal{D}_1, \dots, \mathcal{D}_T\}$
-

bounding box coordinates. A visual sampler then extracts the bounded region from the image. The MLLM subsequently integrates visual tokens from original and cropped images to generate more precise and comprehensive answers. In Sec. 3.1, we detail the automatic preference data generation pipeline. In Sec. 3.2, we describe our Score-DPO (sDPO) for image-level CoT reasoning.

3.1. Preference Data Generation

Given a target model f_{tar} , an evaluator model f_{eval} , and an image-question pair x , we illustrate how to construct n preference data points. The evaluator model f_{eval} is a slightly stronger MLLM than the target model f_{tar} , providing a better assessment of the responses¹. Assume we have T steps in CoT reasoning, we generate preference data for T times on the way, as described in Algorithm 1. At each timestep t (i.e., a reasoning step t), the process includes four stages: Response Generation, Response Evaluation, Pair Construction, and Response Selection.

Response Generation. The goal of this stage is to generate seed bounding boxes and produce intermediate responses to the question using the target model. Here, a “response” refers to any model output at an intermediate step, not necessarily the final answer to the question. We denote the model’s response at timestep t as y_t , with the initial input x represented as y_0 . To create diverse bounding boxes and subsequent responses, we apply stochastic decoding on the target model f_{tar} with n different seeds, resulting in a set of responses y_t^i .

Response Evaluation. This stage evaluates the quality of all generated responses. The evaluator model not only scores each individual response but also counts how this response influences the quality of its next response in the chain. This cumulative evaluation approach helps quantify the impact of each bounded region on the overall reasoning process. Below, we elaborate on the formulation. At

¹Please note that the target MLLM can also be used as the evaluator, validated in Tab. 5.

timestep t , the evaluator assign scores for y_t^i as follows:

$$\begin{aligned} s_{\text{cur}}^i &= f_{\text{eval}}(y_t^i \mid y_{0:t-1}), \\ s_{\text{nxt}}^i &= \mathbb{E}[f_{\text{eval}}(y_{t+1}^i \mid y_{0:t-1}, y_t^i)], \\ s^i &= s_{\text{cur}}^i + \gamma s_{\text{nxt}}^i, \end{aligned} \quad (1)$$

where s_{nxt}^i reflects the impact on the next response and $\gamma > 0$ is a hyperparameter to combine the scores of current and the next response, with $\gamma = 0$ at the last step. We estimate the expectation $\mathbb{E}[\cdot]$ by randomly sampling next responses.

Pair Construction. At each timestep t , we randomly select k (preferred and dis-preferred) pairs from $\{y_t^i\}_{i=1}^n$. For a single pair, we concatenate the preferred response with the past response chain $y_{0:t-1}$ (preserved after $t-1$ timesteps) and get a ‘‘preferred chain’’ denoted as y_t^w , and then we concatenate the dis-preferred response in the same way to get a ‘‘dis-preferred chain’’ denoted as y_t^l . The pair of chains also includes their respective scores, and they are represented as $\{y_w, s_w, y_l, s_l\}$. The overall k pairs of chains compose the preference dataset \mathcal{D}_t .

Response Selection. The abovementioned ‘‘past response chain $y_{0:t-1}$ ’’ is unique and is concatenated by the highest-scoring response at timestep $t-1$ and the preserved chain at timestep $t = 2$, i.e., $y_{0:t-2}$. In other words, when finishing each timestep process, we preserve only the best chain and use it for the next step.

3.2. Unsupervised Learning of UV-COT

Assume the preference dataset \mathcal{D} has been generated across t timesteps, we then optimize the target model with our UV-COT via preference optimization on \mathcal{D} . DPO [1] is widely used in preference learning, and it ranks responses without quantifying preference intensity. In our case of image-level reasoning, key regions vary in influence, necessitating finer differentiation between responses. Therefore, we refine DPO by adjusting the margin to capture the key region’s influence. We name our loss Score-DPO, abbreviated as **sdPO**, as it incorporates the preference score into the optimization. The loss is formulated as:

$$\begin{aligned} \mathcal{L}_{\text{sdPO}}(\theta) &= - \mathbb{E}_{(x, y_w, y_l) \sim \mathcal{D}} \left[\log \sigma \left(\beta \log \frac{\pi_\theta(y_w \mid x)}{\pi_{\text{ref}}(y_w \mid x)} \right. \right. \\ &\quad \left. \left. - \beta \log \frac{\pi_\theta(y_l \mid x)}{\pi_{\text{ref}}(y_l \mid x)} - (g(s_w) - g(s_l)) \right) \right], \end{aligned} \quad (2)$$

where π_θ is the target model, and π_{ref} is its frozen initialization, serving as a reference to constrain deviation from the original model. $g(\cdot) : \mathbb{R} \rightarrow \mathbb{R}$ is a monotonically increasing function that maps preference scores into the logit space of the DPO objective.

To provide a deeper understanding of our sdPO loss, we establish its connection to the standard DPO loss. DPO reformulates reward model training as policy optimization by

Algorithm 2 Iterative learning of UV-COT

- 1: **Input:** Initial target model f_{tar}^1 , evaluator model f_{eval} , $\mathcal{X} = \{\mathcal{X}_1, \dots, \mathcal{X}_m\}$, each \mathcal{X}_i is a subset of image-question query
 - 2: **Output:** f_{tar}^m
 - 3: **for** $i = 1$ to m **do**
 - 4: $\mathcal{D}_i \leftarrow \text{GenerateData}(f_{\text{tar}}^i, f_{\text{eval}}, \mathcal{X}_i)$ \triangleright Algorithm 1
 - 5: $f_{\text{tar}}^{i+1} \leftarrow \text{Train}(f_{\text{tar}}^i, \mathcal{D}_i)$ \triangleright Eq. (2)
 - 6: **end for**
 - 7: **return** f_{tar}^m
-

reparameterizing the reward function in PPO [27]:

$$r(x, y) = \beta \log \frac{\pi_\theta(y \mid x)}{\pi_{\text{ref}}(y \mid x)} + \beta \log Z(x) \quad (3)$$

Using the Bradley-Terry [4] model, the standard DPO aims to minimize the negative log-likelihood of the difference of rewards:

$$\begin{aligned} P(y_w - y_l > 0) &= \sigma(r(x, y_w) - r(x, y_l)) \\ \mathcal{L}_{\text{DPO}} &= -\mathbb{E}_{(x, y_w, y_l) \sim \mathcal{D}} [\log P(y_w - y_l > 0)], \end{aligned} \quad (4)$$

where $\sigma(x) = \frac{1}{1 + \exp(-x)}$ is the sigmoid function.

Let $\Delta_r = g(s_w) - g(s_l)$ and define the Gumbel-distributed random variables $R_w \sim \text{Gumbel}(r(x, y_w), 1)$ and $R_l \sim \text{Gumbel}(r(x, y_l), 1)$. Then, we derive:

$$\begin{aligned} P(R_w - R_l > \Delta_r) &= \sigma(r(x, y_w) - r(x, y_l) - \Delta_r) \\ &= \sigma \left(\beta \log \frac{\pi^*(y_w \mid x)}{\pi_{\text{ref}}(y_w \mid x)} - \beta \log \frac{\pi^*(y_l \mid x)}{\pi_{\text{ref}}(y_l \mid x)} - \Delta_r \right) \end{aligned} \quad (5)$$

This result follows from the definition of Gumbel random variables [1] and the Gumbel-max trick [20]. We provide a detailed proof in the Appendix B. By maximizing the log-likelihood of this objective, we obtain our proposed loss function. The Gumbel distribution models the extreme values of a variable, while Δ_r quantifies the degree of difference between preference pairs. Thus, our loss function explicitly optimizes preference learning by distinguishing not only the order but also the magnitude of preference differences.

Iterative Learning. Standard DPO relies on static preference data during training, which can lead to distributional mismatch between training data and the model’s generated outputs. To mitigate this issue, we adopt an iterative learning approach inspired by [41]. Algorithm 2 outlines the iterative learning process of UV-COT, which incrementally refines a target model through preference learning. The iteration repeats m times, and the total image-question query set \mathcal{X} is evenly divided into m subsets, $\mathcal{X} = \{\mathcal{X}_1, \dots, \mathcal{X}_m\}$, each assigned to one iteration. The process starts with an initial target model f_{tar} , an evaluator model f_{eval} , and \mathcal{X} .

In each iteration i , the algorithm first generates preference data \mathcal{D}_i using the current target model f_{tar}^i and the subset \mathcal{X}_i , using the procedure in Algorithm 1. This newly generated preference data is then used to train the next iteration of the target model f_{tar}^{i+1} using our UV-CoT loss of Eq. (2). The process continues until the final model f_{tar}^m is obtained. By dynamically updating the preference data, our approach ensures that the learned model adapts to its evolving distribution, enhancing training robustness.

4. Experiments

In Sec. 4.1, we outline our experimental setup, including datasets, evaluation metrics, baselines, and implementation details. Sec. 4.2 evaluates UV-CoT on six widely used datasets, demonstrating its superiority over existing baselines. Sec. 4.4 presents ablation studies analyzing impact of key components on overall performance. In Sec. 4.3, we assess the generalization ability of UV-CoT in zero-shot settings across four diverse datasets. In Sec. 4.5, we evaluate the quality of generated bounding boxes across all datasets. In Sec. 4.6, we analyze how our evaluation process reduces task difficulty. In Sec. 4.7, we provide additional analyses on token efficiency, visualization.

4.1. Experimental Setup

Datasets. To generate diverse image-level CoT data, we select nine datasets spanning five domains:

- *Text/Document*: DocVQA [21], TextVQA [29], DUDE [33], and SROIE [10].
- *Chart*: InfographicsVQA [22].
- *General VQA*: Flickr30k [25] and Visual7W [44].
- *Relation Reasoning*: VSR [16] and GQA [11].
- *High-Resolution Image Reasoning*: V* Bench [35].

We follow the procedure in Sec. 3.1 to generate high-quality preference data based on these datasets. Notably, we also provide a model trained on data excluding DUDE, SROIE, and Visual7W, which is used to evaluate zero-shot performance. For details on dataset composition and preprocessing, please refer to Appendix C.1.

Evaluation. Following the evaluation methodology of prior work [18], we use GPT-4o [23] as the evaluator. GPT-4o is prompted to assign a numerical score between 0 and 1, with higher scores indicating better prediction accuracy. Details on prompt design and setup are provided in Appendix C.2.

Baselines We compare our model against five state-of-the-art baselines. Specifically, LLaVA-1.5-7B [17], LLaVA-1.5-13B and OmniLMM-12B serve as strong comprehensive baselines, as they are pretrained on large-scale multimodal data and fine-tuned with high-quality instruction data. OmniLMM-12B is also our evaluator model. Additionally, MiniCPM-o-8B [38] employs an adaptive visual encoding mechanism to capture fine-grained features, improving visual understanding. Finally, Visual-CoT-7B

[28] utilizes labeled data to learn image-level CoT via SFT, achieving competitive performance.

Implementation Details. We use LLaVA-1.5-7B as the target model and OmniLMM-12B as the evaluator. To ensure scalability, we avoid using GPT-4 as the evaluator, preventing constraints imposed by high API costs. Our UV-CoT training follows a two-stage process aligned with the LLaVA-1.5 training framework. In the first stage, the vision encoder and language model weights are frozen while training on image-text caption data. In the second stage, all weights are unfrozen for full training. We implement iterative learning of UV-CoT over four iterations, utilizing a total of 249K preference data pairs. Notably, UV-CoT achieves higher data efficiency than Visual-CoT, which uses 376K data pairs. For each iteration, we train the model with AdamW optimizer for 4 epochs with a learning rate of 5×10^{-7} , $\beta = 0.1$, and a batch size of 8. In total, data generation takes 80 hours and training requires 60 hours, both conducted on an 8xA100 40GB machine. Additionally, we provide a variant UV-CoT trained with extra SFT on 10% of the labeled Visual-CoT data, denoted as UV-CoT (10%).

4.2. Comparisons to State-of-The-Arts

The overall performance comparisons are reported in Tab. 1, leading to the following key observations:

- Both image-level CoT models, Visual-CoT and our UV-CoT, achieve a significant performance gain over all baselines, even outperforming the larger LLaVA-1.5-13B model across all datasets. This highlights the effectiveness of image-level CoT reasoning. Although MiniCPM-o-8B employs crop-and-select strategies to enhance focus on specific image regions, this approach remains limited. In contrast, image-level CoT fully utilizes MLLMs to generate key regions, whereas MiniCPM-o-8B relies on rule-based cropping applied to only a few layers. Nonetheless, MiniCPM-o-8B outperforms LLaVA-1.5-7B by an average of 3.5%, underscoring the importance of explicitly integrating visual cues.
- UV-CoT significantly outperforms OmniLMM-12B by an average of 5.1% across all evaluated datasets. This underscores that our method extend beyond merely distilling knowledge from larger evaluator model. Directly generating accurate bounding boxes is a challenging task for MLLMs, requiring precise spatial understanding and localization. UV-CoT addresses this challenge by reformulating the task to focus on evaluating the final answer, which is inherently more tractable.
- UV-CoT outperforms Visual-CoT-7B on TextVQA (+1.3%) and VSR (+1.6%). Moreover, UV-CoT (10%) surpasses Visual-CoT-7B across four datasets and 2.1% in average, with particularly notable improvements on TextVQA (+2.5%), GQA (+2.2%), and VSR (+2.1%). On the remaining two datasets, UV-CoT (10%) achieves

MLLM	DocVQA	TextVQA	InfographicsVQA	Flickr30k	GQA	VSR	Average
LLaVA-1.5-7B	0.198	0.507	0.131	0.539	0.480	0.504	0.393
LLaVA-1.5-13B	0.225	0.543	0.169	0.607	0.506	0.512	0.427
MiniCPM-o-8B	0.232	0.529	0.175	0.618	0.495	0.521	0.428
OmniLMM-12B	0.254	0.578	0.172	0.621	0.509	0.523	0.443
Visual-CoT-7B (100% label)	0.294	0.673	<u>0.194</u>	0.652	<u>0.546</u>	0.532	<u>0.482</u>
UV-CoT (0% label)	0.265	<u>0.686</u>	0.173	0.632	0.536	<u>0.548</u>	0.473
UV-CoT (10% label)	<u>0.283</u>	0.711	0.198	<u>0.649</u>	0.568	0.553	0.494

Table 1. Overall comparison of different models on six evaluation benchmarks. The **best** result is bold, the second-best is underlined. “%” indicates the percentage of supervised data used in Visual-CoT. By default, our UV-CoT uses only unsupervised data.

MLLM	DUDE	SROIE	Visual7w	Average
LLaVA-1.5-7B	0.165	0.147	0.340	0.217
LLaVA-1.5-13B	0.174	0.159	0.352	0.228
MiniCPM-o-8B	0.182	0.165	0.341	0.229
OmniLMM-12B	0.194	0.166	0.357	0.239
Visual-CoT-7B	0.206	0.181	0.397	0.261
UV-CoT	<u>0.241</u>	<u>0.184</u>	<u>0.432</u>	<u>0.286</u>
UV-CoT*	0.253	0.227	0.455	0.312

Table 2. Zero-shot experiments on DUDE, SROIE and Visual7w. The **best** result is bold, the second-best is underlined. ‘UV-CoT*’ denotes our model trained with additional unlabeled preference data from the three zero-shot datasets.

MLLM	Attributes	GPT4V-hard	OCR	Average
LLaVA-1.5-7B	0.317	0	0.1	0.139
LLaVA-1.5-13B	0.326	0.118	0.133	0.192
MiniCPM-o-8B	0.322	0.118	0.1	0.180
OmniLMM-12B	0.326	0.118	0.167	0.204
Visual-CoT-7B	0.330	0.118	0.593	0.347
UV-CoT	0.352	0.176	0.677	0.402

Table 3. High-resolution image reasoning on V* Bench. The **best** result is bold.

comparable performance to Visual-CoT-7B. Notably, our method is trained on significantly less unlabeled data (249K) than Visual-CoT-7B, which uses 376K labeled CoT data. This success can be attributed to our high-quality preference data generation and the enhanced preference optimization method, which further improves image-level CoT learning.

4.3. Zero-Shot Performance (Generalization)

Comprehensive Zero-Shot. We evaluate our model’s zero-shot image-level CoT capabilities using the test splits of SROIE, DUDE, and Visual7W, without training on these datasets. Since our method does not require labeled data, we can effectively evaluate these datasets even in the ab-

sence of bounding box annotations. Specifically, we train a variant of our model, denoted as UV-CoT*, using preference data that incorporates these datasets. The results are presented in Tab. 2. UV-CoT consistently outperforms all baselines across all zero-shot datasets (2.5% in average), achieving notable improvements on DUDE (+3.5%) and Visual7W (+3.5%), which underscores its strong generalization ability. In contrast, supervised CoT learning, which depends on labeled data, often overfits to specific annotation distributions, limiting its ability to generalize to new tasks. UV-CoT, however, leverages preference optimization by focusing on relative comparisons rather than absolute labels, thereby reducing reliance on specific annotated distributions. Furthermore, UV-CoT* achieves even greater improvements (5.1% in average), with a particularly significant margin on SROIE (+4.6%), demonstrating that our model can effectively learn the image-level CoT process without depending on labeled data. Based on this capability, our method can be easily extended to additional tasks, eliminating the need for costly human annotation.

High-Resolution Image Reasoning. To evaluate the capability in handling challenging high-resolution image reasoning tasks, we test UV-CoT on the V* Bench [35], which comprises 238 images from the SA-1B dataset [12] with an average resolution of 2246×1582. We conduct experiments on three representative tasks—Attributes (object attribute recognition), GPT4V-Hard (complex visual reasoning), and OCR (text recognition)—with the results summarized in Tab. 3. CoT-based methods, UV-CoT (+19.8% on average) and Visual-CoT-7B (+14.3% on average), significantly outperform non-CoT baselines, especially for OCR tasks (more than 50%). And UV-CoT achieves the highest performance across all tasks, surpassing Visual-CoT-7B by 5.5% on average. This illustrates the effectiveness of the visual CoT in high-resolution image reasoning. The superior performance over Visual-CoT-7B further demonstrates that UV-CoT optimizes the visual CoT learning process, enabling fine-grained region-based reasoning.

Model	DocVQA	TextVQA	InfographicsVQA	Flickr30k	GQA	VSR	Average
UV-CoT (10% labels)	0.283	0.711	0.198	0.649	0.568	0.553	0.494
IF: w/o UV-CoT	0.149	0.574	0.160	0.585	0.509	0.522	0.417
IF: UV-CoT w/ G.T. BBox	0.528	0.769	0.504	0.655	0.664	0.585	0.618
Tr: w/ naive DPO	0.258	0.695	0.189	0.623	0.552	0.534	0.475
Tr: w/o iterative learning	0.256	0.671	0.162	0.609	0.523	0.531	0.459
Ge: w/o γ	0.247	0.539	0.152	0.551	0.484	0.460	0.406

Table 4. Ablation study on key components of UV-CoT (10% labeled data). ‘w/o UV-CoT’ denotes standard inference without CoT reasoning. ‘UV-CoT w/ G.T. BBox’ uses annotated ground truth bounding boxes. ‘w/ naive DPO’ applies the standard DPO loss. ‘w/o iterative learning’ generates preference pairs for the entire set of question queries \mathcal{X} in a single pass and trains once. ‘w/o γ ’ evaluates responses with $\gamma = 0$. IF, Tr, and Ge indicate ablations on the inference process, training loss, and data generation, respectively.

4.4. Ablation Studies

This section presents ablation experiments analyzing key components, as shown in Tab. 4.

Image-Level CoT: To evaluate the effectiveness of image-level CoT reasoning, we introduce two variants. w/o UV-CoT removes the CoT reasoning process, relying on direct inference without intermediate reasoning steps. UV-CoT w/ G.T. BBox utilizes ground-truth (GT) bounding boxes in the first step of the CoT process to assess the impact of accurate region selection. Results show that w/o UV-CoT leads to a significant performance drop across all datasets (7.7% in average), demonstrating the effectiveness of our image-level CoT approach. Meanwhile, UV-CoT w/ G.T. BBox serves as an upper bound for our method. In Flickr30k, our model performs on par with UV-CoT w/ G.T. BBox, indicating that it accurately selects key regions. However, in DocVQA and Infographics VQA, UV-CoT w/ G.T. BBox significantly outperforms our method, highlighting the challenge of generating precise bounding boxes. This suggests that our approach has a high upper limit and strong potential. Future work can focus on improving bounding box accuracy, especially for complex tasks.

Preference Optimization: w/ naive DPO applies a standard DPO loss. Its performance deteriorates across all datasets (1.9% in average), with particularly significant drops on DocVQA (2.5%) and Flickr30k (2.6%), highlighting the limitations of standard DPO in image-level CoT learning. This result highlights the advantages of sDPO, which enhances preference differentiation by incorporating scores. The consistent performance gains further validate the accuracy of our preference scores.

Iterative Learning: w/o iterative learning generates preference pairs for the entire set of question queries \mathcal{X} in a single pass and trains once, leading to a significant performance drop (3.5% in average) across evaluated datasets. This underscores the importance of iterative learning in dynamically adapting the preference data distribution to remain aligned with the model’s evolving policy throughout

the training process.

Response Evaluation: We assess the impact of the response evaluation stage by setting $\gamma = 0$, resulting in the w/o γ model. In this setting, the generated preference scores ignore the influence of the next response. This leads to a significant performance drop across all datasets (8.8% in average), particularly on TextVQA (17.2%), highlighting the challenge that MLLMs face in directly evaluating bounding boxes. This result underscores the necessity of incorporating next response in our evaluation method.

4.5. Object Detection Performance

Previous experiments have demonstrated the exceptional performance of our image-level CoT process, highlighting the effectiveness of the generated bounding boxes in improving subsequent answers. However, we remain interested in evaluating the quality of the bounding boxes themselves. To this end, we employ GPT-4o to score the model-generated bounding boxes on both training datasets (Fig. 3 (a)) and zero-shot datasets (Fig. 3 (b)), where best performances are marked with stars. InforVQA is a short for InfographicsVQA. We have the following observations:

- Our UV-CoT outperforms Visual-CoT-7B, achieving higher scores in five out of six training datasets, supporting its superior performance in generating helpful bounding box.
- The bounding box quality is closely related to the final performance. Our model exhibits lower scores (below 0.210) for bounding box generation in DocVQA and InfographicsVQA, correlating with its reduced final scores in these datasets ((below 0.290 in Tab. 1). It underscores the validity of evaluating bounding box quality through its impact on subsequent answers. In addition, this observation explains the performance gap between UV-CoT and UV-CoT w/ G.T. BBoxes in DocVQA and InfographicsVQA, illustrating the upper of our methods.
- Both UV-CoT and UV-CoT* perform better than Visual-CoT-7B across all zero-shot datasets. This demonstrates the strong generalization ability of our method in bound-

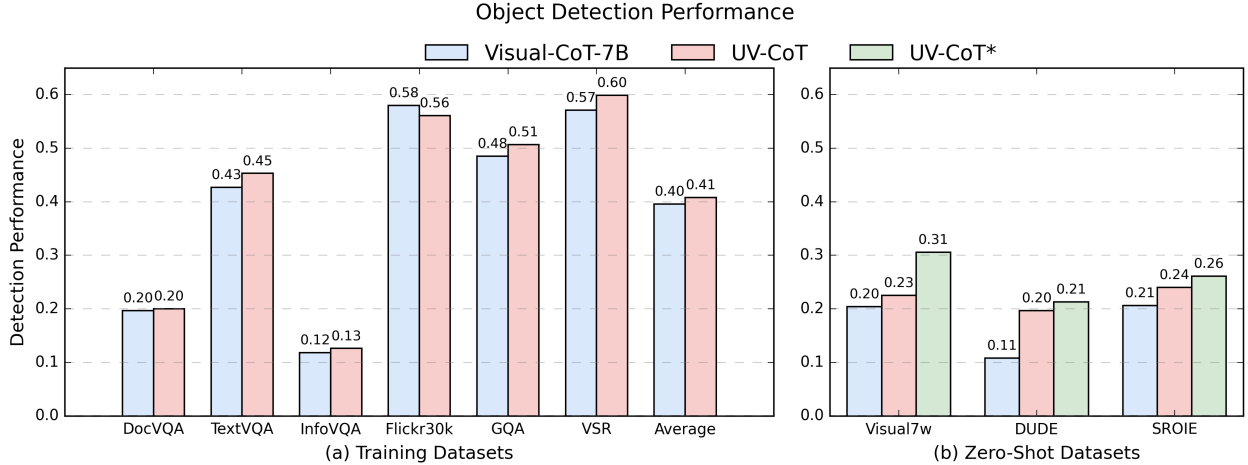


Figure 3. Object detection performance comparisons on (a) training datasets and (b) zero-shot datasets.

Model	DocVQA	TextVQA	InfographicsVQA	Flickr30k	GQA	VSR	Average
OmniLMM-12B	0.254	0.578	0.172	0.621	0.509	0.523	0.443
IF : OmniLMM-12B + CoT	0.305	0.722	0.217	0.675	0.580	0.595	0.516
LLaVA-1.5-7B	0.198	0.507	0.131	0.539	0.480	0.504	0.393
IF : LLaVA-1.5-7B + CoT	0.245	0.577	0.149	0.606	0.530	0.533	0.440
Tr : UV-CoT (Evaluator: self-evaluated)	0.242	0.609	0.153	0.598	0.517	0.526	0.441
Tr : UV-CoT (Evaluator: OmniLMM-12B)	0.265	0.686	0.173	0.632	0.536	0.548	0.473

Table 5. Analysis of evaluator model. + CoT refers to inference assisted by bounding boxes generated by UV-CoT. Self-evaluated denotes using target model as the evaluator during training. IF and Tr indicate experiments conducted on the inference and training process, respectively.

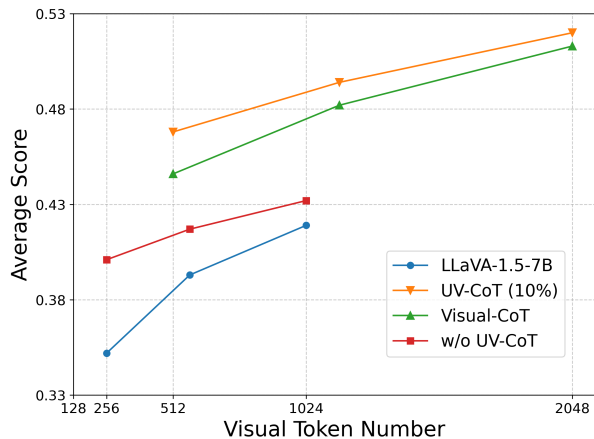


Figure 4. The model performance comparison regarding different sizes of visual tokens.

ing box generation.

4.6. Insight of Evaluator Model

To gain a deeper understanding of the evaluator model, we conduct a series of variant experiments. The key findings, as presented in Tab. 5, are summarized as follows:

- We compare UV-CoT with its self-evaluated variant, where the evaluator model is the same as the target model (initialed with LLaVA-1.5-7B). Although the self-evaluated version exhibits a performance decrease of 3.2% compared to the original UV-CoT, it still outperforms LLaVA-1.5-7B (+4.8% on average) across all evaluated datasets and achieves performance comparable to the larger OmniLMM-12B model (-0.2% on average). This demonstrates that UV-CoT maintains robust performance even under self-evaluation, highlighting its efficiency without requiring larger model scales.
- For OmniLMM-12B and LLaVA-1.5-7B, we incorporate a CoT process using bounding boxes generated by UV-CoT. The CoT-enhanced versions significantly outperform their original counterparts, achieving average performance gains of 4.7% for LLaVA-1.5-7B and 7.4% for OmniLMM-12B across datasets. Remarkably, these models were not fine-tuned for the CoT process, indicating that the bounding box information alone substantially

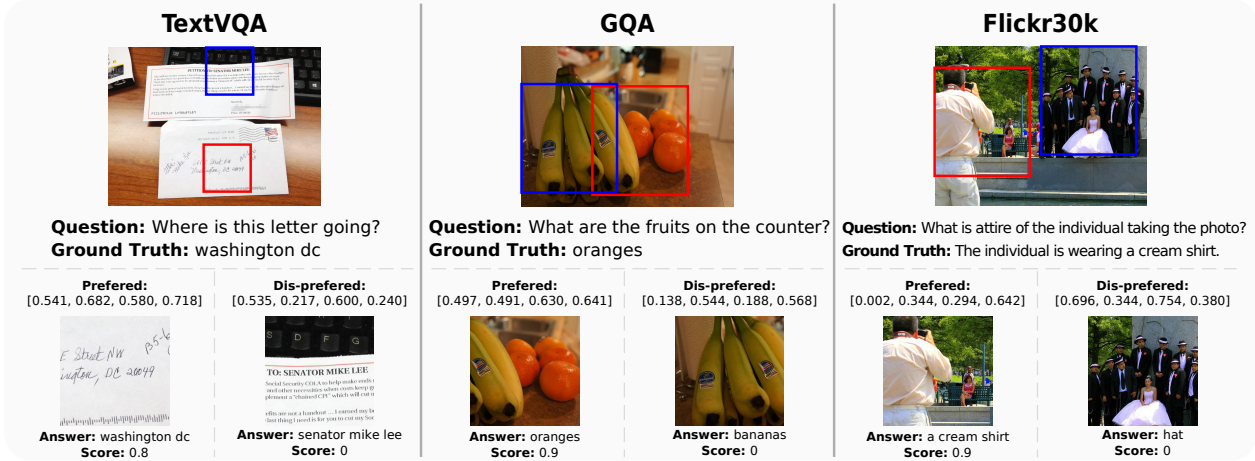


Figure 5. Visualization of preference data generated by Algorithm 1. Preferred bounding boxes are shown in red. Dis-preferred bounding boxes are in blue.

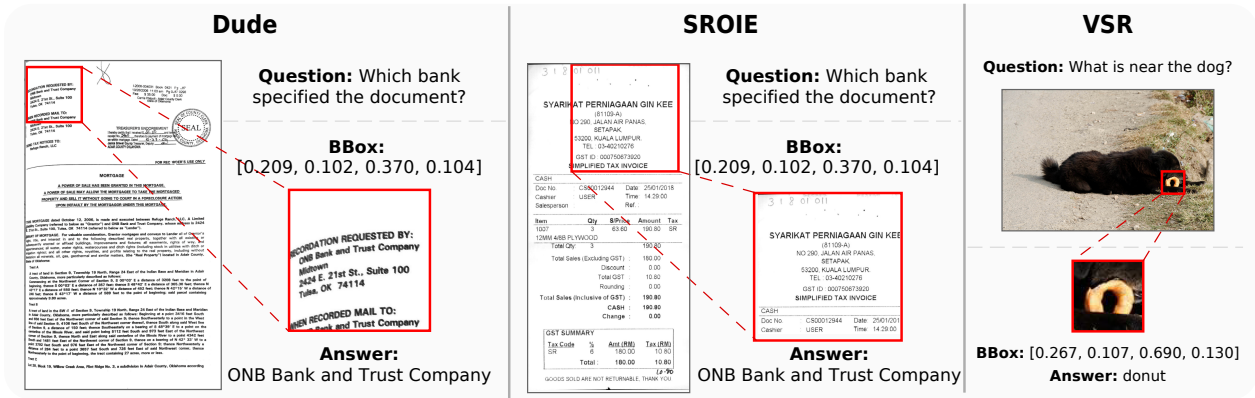


Figure 6. Visualization of our UV-CoT inference. Model-generated bounding boxes are shown in red.

improves performance. This finding underscores that our evaluating process simplifies the task of generating complex spatial annotations, enabling MLLMs to focus on evaluating final answers.

4.7. Other Detailed Analyses

Visual Token Efficiency. Compared to standard answer generation in MLLMs, Visual CoT [28] and our UV-CoT reasoning double the number of visual tokens by processing additional local image regions. To evaluate token efficiency, *i.e.*, performance under the same visual token budget, we resize the input image to different resolutions (224^2 , 336^2 and 448^2) and report the average score of different models in Fig. 4. (1) MLLMs with image-level reasoning (Visual CoT and our UV-CoT) demonstrate better token efficiency than the standard answer generation pipeline. Specifically, they achieve higher performance with 512 visual tokens than the standard pipeline does with 1024 tokens. (2) Our UV-CoT consistently outperforms the Visual CoT pipeline

across all scales, achieving higher average scores due to its well-designed unsupervised learning pipeline. This highlights the token efficiency of our method.

Visualization. This section visualizes preference data and selected cases from our UV-CoT inference. As shown in Fig. 5, given different local regions and their corresponding answers, the evaluator MLLM assigns reasonable scores, validating the effectiveness of our automatic generation and labeling process. In Fig. 6, we present selected reasoning cases with model-generated bounding boxes overlaid. The precision of bounding box detection and the depth of understanding play a crucial role in determining the quality of generated answers.

5. Conclusion

In this work, we propose UV-CoT, a novel framework that enables image-level CoT reasoning in MLLMs via preference optimization techniques. Unlike previous methods that rely on SFT needing large amounts of labeled data, our

approach leverages an unsupervised learning method to refine the model’s ability with image-level CoT using model-generated preference data (which are rough but useful). We address key challenges in preference data generation and effective optimization, ensuring a more adaptive and interpretable reasoning process. Extensive experiments demonstrate that *UV-CoT* achieves state-of-the-art performance, significantly improving visual comprehension in MLLMs on four reasoning datasets. Our findings from extensive experiments highlight the potential of preference learning as a scalable alternative to traditional SFT, enabling more robust and data-efficient multimodal reasoning.

References

- [1] Afra Amini, Tim Vieira, and Ryan Cotterell. Direct preference optimization with an offset. *arXiv preprint arXiv:2402.10571*, 2024. 4, 13
- [2] Mohammad Gheshlaghi Azar, Zhaohan Daniel Guo, Bilal Piot, Remi Munos, Mark Rowland, Michal Valko, and Daniele Calandriello. A general theoretical paradigm to understand learning from human preferences. In *International Conference on Artificial Intelligence and Statistics*, pages 4447–4455. PMLR, 2024. 3
- [3] Jinze Bai, Shuai Bai, Shusheng Yang, Shijie Wang, Sinan Tan, Peng Wang, Junyang Lin, Chang Zhou, and Jingren Zhou. Qwen-vl: A frontier large vision-language model with versatile abilities. *arXiv preprint arXiv:2308.12966*, 2023. 1, 2
- [4] Ralph Allan Bradley and Milton E Terry. Rank analysis of incomplete block designs: I. the method of paired comparisons. *Biometrika*, 39(3/4):324–345, 1952. 4
- [5] Herbert Aron David. *The method of paired comparisons*. London, 1963. 13
- [6] Kawin Ethayarajh, Winnie Xu, Niklas Muennighoff, Dan Jurafsky, and Douwe Kiela. Kto: Model alignment as prospect theoretic optimization. *arXiv preprint arXiv:2402.01306*, 2024. 3
- [7] Guhao Feng, Bohang Zhang, Yuntian Gu, Haotian Ye, Di He, and Liwei Wang. Towards revealing the mystery behind chain of thought: a theoretical perspective. *Advances in Neural Information Processing Systems*, 36:70757–70798, 2023. 2
- [8] Guhao Feng, Bohang Zhang, Yuntian Gu, Haotian Ye, Di He, and Liwei Wang. Towards revealing the mystery behind chain of thought: a theoretical perspective. *Advances in Neural Information Processing Systems*, 36, 2024. 1
- [9] Mingxin Huang, Yuliang Liu, Dingkan Liang, Lianwen Jin, and Xiang Bai. Mini-monkey: Alleviating the semantic sawtooth effect for lightweight mllms via complementary image pyramid. *arXiv preprint arXiv:2408.02034*, 2024. 1
- [10] Zheng Huang, Kai Chen, Jianhua He, Xiang Bai, Dimosthenis Karatzas, Shijian Lu, and CV Jawahar. Icdar2019 competition on scanned receipt ocr and information extraction. In *2019 International Conference on Document Analysis and Recognition (ICDAR)*, pages 1516–1520. IEEE, 2019. 5, 14
- [11] Drew A Hudson and Christopher D Manning. Gqa: A new dataset for real-world visual reasoning and compositional question answering. In *Proceedings of the IEEE/CVF conference on computer vision and pattern recognition*, pages 6700–6709, 2019. 5, 14
- [12] Alexander Kirillov, Eric Mintun, Nikhila Ravi, Hanzi Mao, Chloe Rolland, Laura Gustafson, Tete Xiao, Spencer Whitehead, Alexander C Berg, Wan-Yen Lo, et al. Segment anything. In *Proceedings of the IEEE/CVF international conference on computer vision*, pages 4015–4026, 2023. 6, 14
- [13] Takeshi Kojima, Shixiang Shane Gu, Machel Reid, Yutaka Matsuo, and Yusuke Iwasawa. Large language models are zero-shot reasoners. *Advances in neural information processing systems*, 35:22199–22213, 2022. 1, 2
- [14] Xin Lai, Zhuotao Tian, Yukang Chen, Senqiao Yang, Xiangru Peng, and Jiaya Jia. Step-dpo: Step-wise preference optimization for long-chain reasoning of llms. *arXiv preprint arXiv:2406.18629*, 2024. 3
- [15] Harrison Lee, Samrat Phatale, Hassan Mansoor, Kellie Ren Lu, Thomas Mesnard, Johan Ferret, Colton Bishop, Ethan Hall, Victor Carbune, and Abhinav Rastogi. Rlaif: Scaling reinforcement learning from human feedback with ai feedback. 2023. 3
- [16] Fangyu Liu, Guy Emerson, and Nigel Collier. Visual spatial reasoning. *Transactions of the Association for Computational Linguistics*, 11:635–651, 2023. 5, 14
- [17] Haotian Liu, Chunyuan Li, Yuheng Li, and Yong Jae Lee. Improved baselines with visual instruction tuning. In *Proceedings of the IEEE/CVF Conference on Computer Vision and Pattern Recognition*, pages 26296–26306, 2024. 1, 5
- [18] Haotian Liu, Chunyuan Li, Qingyang Wu, and Yong Jae Lee. Visual instruction tuning. *Advances in neural information processing systems*, 36, 2024. 1, 5
- [19] Haoyu Lu, Wen Liu, Bo Zhang, Bingxuan Wang, Kai Dong, Bo Liu, Jingxiang Sun, Tongzheng Ren, Zhuoshu Li, Hao Yang, et al. Deepseek-vl: towards real-world vision-language understanding. *arXiv preprint arXiv:2403.05525*, 2024. 2
- [20] Chris J. Maddison and Danny Tarlow. Gumbel machinery, 2017. Available online. 4, 13
- [21] Minesh Mathew, Dimosthenis Karatzas, and CV Jawahar. Docvqa: A dataset for vqa on document images. In *Proceedings of the IEEE/CVF winter conference on applications of computer vision*, pages 2200–2209, 2021. 5, 14, 15
- [22] Minesh Mathew, Viraj Bagal, Rubèn Tito, Dimosthenis Karatzas, Ernest Valveny, and CV Jawahar. Infographicvqa. In *Proceedings of the IEEE/CVF Winter Conference on Applications of Computer Vision*, pages 1697–1706, 2022. 5, 14, 15
- [23] OpenAI. Chatgpt, 2023. Accessed: Mar. 4, 2025. 5
- [24] Richard Yuanzhe Pang, Weizhe Yuan, He He, Kyunghyun Cho, Sainbayar Sukhbaatar, and Jason Weston. Iterative reasoning preference optimization. *Advances in Neural Information Processing Systems*, 37:116617–116637, 2025. 3
- [25] Bryan A Plummer, Liwei Wang, Chris M Cervantes, Juan C Caicedo, Julia Hockenmaier, and Svetlana Lazebnik. Flickr30k entities: Collecting region-to-phrase correspondences for richer image-to-sentence models. In *Proceedings of the IEEE international conference on computer vision*, pages 2641–2649, 2015. 5, 14
- [26] Rafael Rafailov, Archit Sharma, Eric Mitchell, Christopher D Manning, Stefano Ermon, and Chelsea Finn. Direct preference optimization: Your language model is secretly a reward model. *Advances in Neural Information Processing Systems*, 36:53728–53741, 2023. 3
- [27] John Schulman, Filip Wolski, Prafulla Dhariwal, Alec Radford, and Oleg Klimov. Proximal policy optimization algorithms. *arXiv preprint arXiv:1707.06347*, 2017. 4, 13
- [28] Hao Shao, Shengju Qian, Han Xiao, Guanglu Song, Zhuofan Zong, Letian Wang, Yu Liu, and Hongsheng Li. Visual

- cot: Advancing multi-modal language models with a comprehensive dataset and benchmark for chain-of-thought reasoning. *Advances in Neural Information Processing Systems*, 37:8612–8642, 2025. 1, 2, 5, 9, 14
- [29] Amanpreet Singh, Vivek Natarajan, Meet Shah, Yu Jiang, Xinlei Chen, Dhruv Batra, Devi Parikh, and Marcus Rohrbach. Towards vqa models that can read. In *Proceedings of the IEEE/CVF conference on computer vision and pattern recognition*, pages 8317–8326, 2019. 5, 14
- [30] Zhiqing Sun, Sheng Shen, Shengcao Cao, Haotian Liu, Chunyuan Li, Yikang Shen, Chuang Gan, Liang-Yan Gui, Yu-Xiong Wang, Yiming Yang, et al. Aligning large multi-modal models with factually augmented rlhf. *arXiv preprint arXiv:2309.14525*, 2023. 3
- [31] Fuxiao Tan, Pengfei Yan, and Xinping Guan. Deep reinforcement learning: From q-learning to deep q-learning. In *Neural Information Processing: 24th International Conference, ICONIP 2017, Guangzhou, China, November 14–18, 2017, Proceedings, Part IV 24*, pages 475–483. Springer, 2017. 2
- [32] Hugo Touvron, Thibaut Lavril, Gautier Izacard, Xavier Martinet, Marie-Anne Lachaux, Timothée Lacroix, Baptiste Rozière, Naman Goyal, Eric Hambro, Faisal Azhar, et al. Llama: Open and efficient foundation language models. *arXiv preprint arXiv:2302.13971*, 2023. 2
- [33] Jordy Van Landeghem, Rubèn Tito, Łukasz Borchmann, Michał Pietruszka, Paweł Joziak, Rafał Powalski, Dawid Jurkiewicz, Mickaël Coustaty, Bertrand Anckaert, Ernest Valveny, et al. Document understanding dataset and evaluation (dude). In *Proceedings of the IEEE/CVF International Conference on Computer Vision*, pages 19528–19540, 2023. 5, 14
- [34] Jason Wei, Xuezhi Wang, Dale Schuurmans, Maarten Bosma, Fei Xia, Ed Chi, Quoc V Le, Denny Zhou, et al. Chain-of-thought prompting elicits reasoning in large language models. *Advances in neural information processing systems*, 35:24824–24837, 2022. 1, 2
- [35] Penghao Wu and Saining Xie. V?: Guided visual search as a core mechanism in multimodal llms. In *Proceedings of the IEEE/CVF Conference on Computer Vision and Pattern Recognition*, pages 13084–13094, 2024. 5, 6, 14
- [36] Guowei Xu, Peng Jin, Li Hao, Yibing Song, Lichao Sun, and Li Yuan. Llava-o1: Let vision language models reason step-by-step. *arXiv preprint arXiv:2411.10440*, 2024. 1, 2
- [37] Zhengyuan Yang, Linjie Li, Jianfeng Wang, Kevin Lin, Ehsan Azarnasab, Faisal Ahmed, Zicheng Liu, Ce Liu, Michael Zeng, and Lijuan Wang. Mm-react: Prompting chatgpt for multimodal reasoning and action. *arXiv preprint arXiv:2303.11381*, 2023. 1, 2
- [38] Yuan Yao, Tianyu Yu, Ao Zhang, Chongyi Wang, Junbo Cui, Hongji Zhu, Tianchi Cai, Haoyu Li, Weilin Zhao, Zhihui He, et al. Minicpm-v: A gpt-4v level mllm on your phone. *arXiv preprint arXiv:2408.01800*, 2024. 5
- [39] Tianyu Yu, Jinyi Hu, Yuan Yao, Haoye Zhang, Yue Zhao, Chongyi Wang, Shan Wang, Yinxv Pan, Jiao Xue, Dahai Li, et al. Reformulating vision-language foundation models and datasets towards universal multimodal assistants. *arXiv preprint arXiv:2310.00653*, 2023. 1
- [40] Tianyu Yu, Yuan Yao, Haoye Zhang, Taiwan He, Yifeng Han, Ganqu Cui, Jinyi Hu, Zhiyuan Liu, Hai-Tao Zheng, Maosong Sun, et al. Rlhf-v: Towards trustworthy mllms via behavior alignment from fine-grained correctional human feedback. In *Proceedings of the IEEE/CVF Conference on Computer Vision and Pattern Recognition*, pages 13807–13816, 2024. 3
- [41] Tianyu Yu, Haoye Zhang, Yuan Yao, Yunkai Dang, Da Chen, Xiaoman Lu, Ganqu Cui, Taiwan He, Zhiyuan Liu, Tat-Seng Chua, et al. Rlaif-v: Aligning mllms through open-source ai feedback for super gpt-4v trustworthiness. *arXiv preprint arXiv:2405.17220*, 2024. 3, 4
- [42] Zhuosheng Zhang, Aston Zhang, Mu Li, and Alex Smola. Automatic chain of thought prompting in large language models. *arXiv preprint arXiv:2210.03493*, 2022. 1, 2
- [43] Zhuosheng Zhang, Aston Zhang, Mu Li, Hai Zhao, George Karypis, and Alex Smola. Multimodal chain-of-thought reasoning in language models. *arXiv preprint arXiv:2302.00923*, 2023. 1, 2
- [44] Yuke Zhu, Oliver Groth, Michael Bernstein, and Li Fei-Fei. Visual7w: Grounded question answering in images. In *Proceedings of the IEEE conference on computer vision and pattern recognition*, pages 4995–5004, 2016. 5, 14
- [45] Daniel M Ziegler, Nisan Stiennon, Jeffrey Wu, Tom B Brown, Alec Radford, Dario Amodei, Paul Christiano, and Geoffrey Irving. Fine-tuning language models from human preferences. *arXiv preprint arXiv:1909.08593*, 2019. 3

A. Outline

We begin by presenting an overview of our Appendix.

- **Section B: Framework Details.** We provide a detailed explanation on the connection between our UV-CoT and DPO.
- **Section C: Implement Details.** We describe the specifics of our dataset, and evaluation methodology.
- **Section D: Limitations.** We analysis the constraints and challenges of our approach.
- **Section E: Potential negative societal impacts.** We discuss possible negative consequences and ethical considerations associated with our work.

B. Connection between UV-CoT and DPO

B.1. Loss Function Formulation

To better captures the impact of key regions, we introduce a preference-weighted optimization approach. The loss function for UV-CoT is defined as follows:

$$\mathcal{L}_{sDPO}(\theta) = -\mathbb{E}_{(x, y_w, y_l) \sim \mathcal{D}} \left[\log \sigma \left(\beta \log \frac{\pi_\theta(y_w | x)}{\pi_{\text{ref}}(y_w | x)} - \beta \log \frac{\pi_\theta(y_l | x)}{\pi_{\text{ref}}(y_l | x)} - (g(s_w) - g(s_l)) \right) \right]. \quad (6)$$

where π_θ is the target policy model being optimized, π_{ref} is the frozen reference model, constraining deviations from the initial policy, $g : \mathbb{R} \rightarrow \mathbb{R}$ is a monotonically increasing function mapping preference scores s_w and s_l (for winning and losing responses y_w and y_l) into the logit space, β is a temperature parameter, \mathcal{D} represents the dataset distribution over input-output pairs (x, y_w, y_l) .

This formulation extends the DPO framework by incorporating preference differences $g(s_w) - g(s_l)$, which reflect the utility of key regions identified by UV-CoT.

B.2. DPO Background and Reparameterization

DPO reformulates reward model training as a policy optimization problem by reparameterizing the reward function from Proximal Policy Optimization (PPO) [27]:

$$r(x, y) = \beta \log \frac{\pi_\theta(y | x)}{\pi_{\text{ref}}(y | x)} + \beta \log Z(x), \quad (7)$$

where $Z(x)$ is the partition function. Substituting this into the Bradley-Terry preference model [5] yields:

$$\begin{aligned} p(y_w \succ y_l) &= \sigma(r(x, y_w) - r(x, y_l)) \\ &= \sigma \left(\beta \log \frac{\pi_\theta(y_w | x)}{\pi_{\text{ref}}(y_w | x)} - \beta \log \frac{\pi_\theta(y_l | x)}{\pi_{\text{ref}}(y_l | x)} \right), \end{aligned} \quad (8)$$

where σ is the sigmoid function. Maximizing the log-likelihood of this preference model leads to the naive DPO loss:

$$\mathcal{L}_{\text{DPO}}(\theta) = -\mathbb{E}_{(x, y_w, y_l) \sim \mathcal{D}} \left[\log \sigma \left(\beta \log \frac{\pi_\theta(y_w | x)}{\pi_{\text{ref}}(y_w | x)} - \beta \log \frac{\pi_\theta(y_l | x)}{\pi_{\text{ref}}(y_l | x)} \right) \right]. \quad (9)$$

B.3. Derivation with Gumbel Distribution

To incorporate preference-weighted optimization, we define $\Delta_r = g(s_w) - g(s_l)$ and introduce Gumbel-distributed random variables $R_w \sim \text{Gumbel}(r(x, y_w), 1)$ and $R_l \sim \text{Gumbel}(r(x, y_l), 1)$. The probability that the winning response is preferred, adjusted by the preference gap, is:

$$\begin{aligned} P(R_w - R_l > \Delta_r) &= \sigma(r(x, y_w) - r(x, y_l) - \Delta_r) \\ &= \sigma \left(\beta \log \frac{\pi^*(y_w | x)}{\pi_{\text{ref}}(y_w | x)} - \beta \log \frac{\pi^*(y_l | x)}{\pi_{\text{ref}}(y_l | x)} - \Delta_r \right). \end{aligned} \quad (10)$$

This result leverages the Gumbel-max trick [20], with a similar derivation found in ODT0 [1].

B.4. Proof of Gumbel-Based Preference

We first prove the foundational probability $P(R_w - R_l > 0) = \sigma(\Delta_{\hat{r}_\theta})$, where $\Delta_{\hat{r}_\theta} = r_\theta(x, y_w) - r_\theta(x, y_l)$.

Proof: Define the random variable $I = \arg \max_{l, w} \{R_l, R_w\}$. The goal is to show:

$$P(I = w) = \frac{\exp(\hat{r}_\theta(x, y_w))}{\exp(\hat{r}_\theta(x, y_w)) + \exp(\hat{r}_\theta(x, y_l))}. \quad (11)$$

For notation simplicity, let $\hat{r}_w = \hat{r}_\theta(x, y_w)$, $\hat{r}_l = \hat{r}_\theta(x, y_l)$, and $g_{\hat{r}_w} \sim \text{Gumbel}(\hat{r}_w, 1)$. Then:

$$\begin{aligned} P(I = w) &= \mathbb{E}_{m \sim g_{\hat{r}_w}} [P(R_l < m)] \\ &= \int_{-\infty}^{\infty} \exp(-m) \cdot \exp(-\exp(\hat{r}_l - m)) \cdot \exp(\hat{r}_w) dm, \end{aligned} \quad (12)$$

(13)

where the integral accounts for the Gumbel CDF. Let $Z = \exp(\hat{r}_w) + \exp(\hat{r}_l)$. The expression simplifies to:

$$P(I = w) = \frac{\exp(\hat{r}_w)}{Z} = \frac{\exp(\hat{r}_\theta(x, y_w))}{\exp(\hat{r}_\theta(x, y_w)) + \exp(\hat{r}_\theta(x, y_l))}, \quad (14)$$

proving Equation (11). Extending this to the preference gap Δ_r , we derive:

$$\begin{aligned} P(R_w - R_l > \Delta_r) &= 1 - \mathcal{F}(\Delta_r) \\ &= \frac{1}{2} - \frac{1}{2} \tanh \left(\frac{\Delta_r - \Delta_{\hat{r}_\theta}}{2} \right) \\ &= \sigma(\Delta_{\hat{r}_\theta} - \Delta_r), \end{aligned} \quad (15)$$

Table 6. The details of the datasets, which spans five distinct domains and includes various source datasets.

Domain	Source Dataset	Size	Dataset Description
Text/Doc	TextVQA	16k	Images with text
	DocVQA	35k	Doc images
	DUDE	15k	Doc images
	SROIE	4k	Invoice images
Chart	InfographicsVQA	15k	Infographic images
General VQA	Visual7W	43k	Images
	Flickr30k	136k	Images
Relation Reasoning	VSR	3k	Images
	GQA	88k	Images
High-Resolution	V* Bench	238	Images

where $\Delta_{\hat{r}_\theta} = r_\theta(x, y_w) - r_\theta(x, y_l)$. This completes the derivation of the UV-CoT loss in Equation (6).

C. Implement Details

C.1. Datasets

To generate diverse and comprehensive image-level Chain-of-Thought (CoT) data for training Multimodal Large Language Models (MLLMs), we select nine source datasets spanning four distinct domains: Text/Doc, General Visual Question Answering (VQA), Charts, and Relation Reasoning. These domains are chosen to ensure a broad representation of visual reasoning tasks, enabling the model to develop robust CoT capabilities across varied contexts.

Before performing preference optimization, we conduct Supervised Fine-Tuning (SFT) using 10% of the labeled Visual-CoT dataset, which corresponds to approximately 25k samples, as detailed in Tab. 6. This subset is chosen to balance computational efficiency with sufficient exposure to diverse reasoning patterns, resulting in a model we denote as UV-CoT (10%). Following SFT, we perform preference optimization using a total of 249k preference data points, curated from the same nine datasets. The preference data is generated by ranking model outputs for each dataset, ensuring that the distribution across domains mirrors that of Visual-CoT [28]. Specifically, for each dataset, we maintain roughly the same proportion of preference pairs as in Visual-CoT (e.g., Text/Doc datasets contribute approximately 50% of the data, consistent with their representation in our dataset). This approach ensures that UV-CoT benefits from a balanced and comprehensive preference optimization process, enhancing its ability to prioritize key regions in visual reasoning tasks.

As shown in Tab. 6, we provide a detailed introduction to the datasets we used. For the Text/Doc domain, we include four datasets focusing on text recogni-

tion and comprehension in diverse document and image formats: DocVQA [21], TextVQA [29], DUDE [33], and SROIE [10]. These datasets provide rich text-based reasoning scenarios, such as extracting information from invoices (SROIE) or answering questions about document content (DocVQA), which are crucial for generating CoT data that involves step-by-step text interpretation.

In the General VQA domain, we select Flickr30k [25] and Visual7W [44]. These datasets are well-suited for general visual question answering, as they contain diverse images paired with questions that require understanding both visual content and textual prompts, facilitating the creation of CoT data for general reasoning tasks.

For the Charts domain, we use the InfographicsVQA dataset [22], which consists of high-resolution infographics. This dataset is particularly advantageous for training MLLMs to localize and interpret specific regions in charts, enabling the generation of CoT data that involves reasoning about data visualization elements such as legends, labels, and trends.

In the Relation Reasoning domain, we select VSR [16] and GQA [11]. These datasets are rich in spatial relational information among objects in images, making them ideal for constructing CoT data that focus on reasoning about object relationships, such as identifying relative positions or dependencies in a scene.

For high-resolution image reasoning, we use V* Bench [35], which comprises 238 images from the SA-1B dataset [12] with an average resolution of 2246×1582 .

C.2. Evaluation

We utilize GPT-4o to assess the performance of our model due to its superior reasoning capabilities and adopt an evaluation prompt to. The prompt template is like:

Evaluating Prompt Template

You are a helpful and precise assistant for checking the quality of the answer, you need to give a score to the model's answer by referring to the standard answer, based on the given question. The full score is 1 point and the minimum score is 0 points. Please output the score in the form 'score: <score >'. The evaluation criteria require that the closer the model's answer is to the standard answer, the higher the score.

The meaning score, ranging from 0 to 1, reflects the semantic relevance of the model's responses to the given prompts.

D. Limitations

While our UV-CoT model demonstrates high performance across most evaluated datasets, it encounters challenges in accurately identifying anchor boxes on certain datasets, notably DocVQA [21] and InfographicsVQA [22]. These difficulties may arise due to the complex layouts, variable text densities, and noisy annotations prevalent in these datasets, which complicate the localization of relevant regions. In contrast, the ground truth (GT) boxes achieve exceptional performance on these datasets, suggesting that our model has significant untapped potential. Future research could explore advanced anchor box detection algorithms, such as incorporating adaptive thresholding or multi-scale feature extraction, to address these limitations and enhance the model's robustness across diverse visual domains.

E. Potential negative societal impacts

The potential negative societal impacts of our work align with those of other MLLMs and LLMs. While the development of UV-CoT and MLLMs advances AI capabilities, it also introduces several risks. These include heightened privacy concerns, the reinforcement of existing biases, the spread of misinformation, job displacement due to automation, and ethical challenges related to accountability, transparency, and informed consent. Addressing these issues requires responsible deployment, continuous monitoring, and the implementation of safeguards to mitigate unintended consequences.